nanomaterials

MDPI

Article

Heterostructured g-CN/TiO_2 Photocatalysts Prepared by Thermolysis of g-CN/MIL-125(Ti) Composites for Efficient Pollutant Degradation and Hydrogen Production

Batukhan Tatykayev [1,2], Bilel Chouchene [1], Lavinia Balan [3], Thomas Gries [4], Ghouti Medjahdi [4], Emilien Girot [1], Bolat Uralbekov [2] and Raphaël Schneider [1,*]

1 CNRS, LRGP, Université de Lorraine, F-54000 Nancy, France; b.tatykayev@gmail.com (B.T.); bilel.chouchene@univ-lorraine.fr (B.C.); emilien.girot@univ-lorraine.fr (E.G.)
2 Department of General and Inorganic Chemistry, Al-Farabi Kazakh National University, Al-Farabi Av., 71, Almaty 050040, Kazakhstan; bulat.ural@gmail.com
3 Conditions Extrêmes et Matériaux: Haute Température et Irradiation, UPR 3079 CNRS, Site Haute Température, 1D avenue de la Recherche Scientifique, 45071 Orléans, France; lavinia.balan@cnrs-orleans.fr
4 CNRS, IJL, Université de Lorraine, F-54000 Nancy, France; thomas.gries@univ-lorraine.fr (T.G.); ghouti.medjahdi@univ-lorraine.fr (G.M.)
* Correspondence: raphael.schneider@univ-lorraine.fr; Tel.: +33-3-78-74-37

Received: 18 June 2020; Accepted: 13 July 2020; Published: 16 July 2020

Abstract: Photocatalysts composed of graphitic carbon nitride (g-CN) and TiO_2 were efficiently prepared by thermolysis of the MIL-125(Ti) metal organic framework deposited on g-CN. The heterojunction between the 12 nm-sized TiO_2 nanoparticles and g-CN was well established and the highest photocatalytic activity was observed for the g-CN/TiO_2 (3:1) material. The g-CN/TiO_2 (3:1) composite exhibits high visible light performances both for the degradation of pollutants like the Orange II dye or tetracycline but also for the production of hydrogen (hydrogen evolution rate (HER) up to 1330 $\mu molh^{-1}g^{-1}$ and apparent quantum yield of 0.22% using NiS as a cocatalyst). The improved visible light performances originate from the high specific surface area of the photocatalyst (86 m^2g^{-1}) and from the efficient charge carriers separation as demonstrated by photoluminescence, photocurrent measurements, and electrochemical impedance spectroscopy. The synthetic process developed in this work is based on the thermal decomposition of metal organic framework deposited on a graphitic material and holds huge promise for the preparation of porous heterostructured photocatalysts.

Keywords: graphitic carbon nitride; MIL-125(Ti); titanium dioxide; heterostructured photocatalysts

1. Introduction

The assembly of semiconductors into heterostructures has recently attracted considerable attention due to the numerous photocatalytic applications of these materials like detoxification of water or solar-to-chemical energy conversion [1–5]. In heterostructured photocatalysts, both the efficient spatial separation of charge carriers and the enhanced light absorption allow to boost the catalytic activity compared to the individual components due to a synergistic effect.

Titanium dioxide TiO_2 is one of the most important photocatalyst and has been widely used for environmental applications or water splitting [6–11]. However, the photocatalytic performances of TiO_2 are limited by its wide bandgap energy (ca. 3.2 eV) which restricts its photoactivation to UV light and by its modest charge transport efficiency. Graphitic carbon nitride (g-CN) is an organic layered

semiconductor composed of carbon and nitrogen with an energy bandgap of ca. 2.7 eV and exhibiting high chemical, thermal and photostability [1,12–14]. As TiO_2, bulk g-CN suffers from several drawbacks including the fast recombination of photogenerated charge carriers and a low specific surface area (less than 10 m^2g^{-1}), which decrease its catalytic performance [1,12–14]. However, the conduction band of g-CN is located at ca. −1.3 eV at pH 7 vs. NHE and is more negative than that of TiO_2 [15,16], which allows photogenerated electrons to be efficiently transferred from the conduction band of g-CN to the conduction band of TiO_2. This decrease of the photogenerated electron-hole pair's recombination allows significant improvements in the photocatalytic performance of g-CN/TiO_2 composites.

Various methods have been developed for the preparation of g-CN/TiO_2 heterostructured photocatalyts. The most commonly used process is the ultrasonication or the mechanical mixing of pre-formed TiO_2 and g-CN followed by a heat treatment at temperatures varying from 300 to 500 °C to hybridize their energy levels [17–21]. To improve the interfacial connection between TiO_2 and g-CN and thus the delocalization of charge carriers, synthetic methods involving the deposition of Ti precursors like $Ti(On\text{-}Bu)_4$ at the surface of exfoliated g-CN followed a hydro- or a solvothermal reaction and a calcination have been reported [22–25]. The reverse process including the generation of g-CN by calcination of N-rich precursors (melamine and/or cyanuric acid) in the presence of TiO_2 nanoparticles or titanate nanotubes has also been investigated [26–32]. Finally, the vapor phase deposition of g-CN at the surface of TiO_2 [33] or the surface modification of g-CN with chloroacetic acid to increase the association with TiO_2 have also been reported [34].

In recent years, the preparation of porous metal oxides derived from metal organic frameworks (MOFs) has gained high interest for environmental and energy-related applications. After thermolysis, the textural properties of MOFs are partially transferred to the porous metal oxide exposing a high density of active sites and in which charge carriers easily diffuse to the surface of the photocatalyst [35]. Using the NH_2-MIL-125(Ti) as starting MOF, this strategy has successfully been used to prepare photocatalysts associating TiO_2 nanoparticles deposited on carbon or associated to MoS_2 [36–38]. MIL-125(Ti) is a MOF responding to the formula $Ti_8O_8(OH)_4[O_2C\text{-}C_6H_4\text{-}CO_2]_6$ and exhibiting a well-defined porosity and high specific surface area (ca. 1700 m^2g^{-1}) [39]. MIL-125(Ti) is a good precursor of TiO_2 nanocrystals [40,41] that demonstrated a good photocatalytic activity for CO_2 reduction, As(III) oxidation or pollutant degradation [42–48].

Herein, a novel synthetic process using in the key step the thermolysis of g-CN/MIL-125(Ti) assemblies was developed to prepare highly active g-CN/TiO_2 photocatalysts. The mass ratio of g-CN to TiO_2 was varied and the highest photocatalytic activity was obtained for the g-CN/TiO_2 (3:1) material. The g-CN/TiO_2 photocatalyst was not only demonstrated to be highly efficient for the degradation of pollutants in aqueous phase but also for H_2 photoproduction using NiS as co-catalyst.

2. Materials and Methods

2.1. Chemicals

Terephthalic acid (98%, Sigma), titanium (IV) propoxide (98%, Sigma), melamine (99%, Sigma), dimethylformamide (DMF) (99.9%, Sigma), Orange II sodium salt (microscopy grade, Sigma), tetracycline hydrochloride (Bioreagent, Sigma), glycerol (>99.5%, Sigma), methanol (99.9%, Sigma) and ethanol (anhydrous, Sigma) were used as received.

2.2. Synthesis of MIL-125(Ti)

Terephthalic acid (3 g, 18.28 mmol) was dissolved in 54 mL of anhydrous DMF and 6 mL MeOH by magnetic stirring for 15 min. To the obtained solution was added titanium (IV) propoxide (3.6 mL, 13.08 mmol) and the mixture was stirred for 30 min under argon. Then, the solution was transferred into a 100 mL Teflon-lined stainless autoclave and heated in an oven at 150 °C for 48 h. After cooling to room temperature, MIL-125(Ti) particles were collected by centrifugation (4000 rpm for 15 min),

washed with DMF (3 × 30 mL), with MeOH (3 × 30 mL) and finally dried at 70 °C overnight. A typical synthesis affords 1.86 g of a white powder.

2.3. Synthesis of Bulk g-CN

Melamine (5 g) was placed into a covered ceramic crucible and heated under air at 500 °C at a rate of 10 °C min^{-1} and then maintained at 500 °C for 2 h. The yellow powder obtained (1.75 g) was ground in an agate mortar.

2.4. Exfoliation of g-CN

Bulk g-CN (0.5 g) was dispersed in 80 mL water and ultrasonicated for 60 min using a Sonic Dismembrator 550 (Fisher Scientific, Illkirch, France). Next, the obtained white-yellow dispersion was centrifuged for 30 min at 5000 rpm, the precipitate collected, washed with EtOH (30 mL) and dried at 70 °C overnight.

2.5. Preparation of g-CN/TiO_2 Photocatalysts

A representative synthesis of the g-CN/TiO_2 (3:1) photocatalyst is described. Exfoliated g-CN (180 mg) and MIL-125(Ti) (120 mg) were dispersed in 5 mL water and the mixture sonicated for 30 min. After centrifugation (4000 rpm for 15 min), the powder was washed with EtOH (30 mL) and dried at 70 °C for 3 h. Then, the powder was placed into a covered ceramic crucible, heated under air at 450 °C at a rate of 10 °C min^{-1} and maintained at 450 °C for 2 h before cooling. The g-CN/TiO_2 composites were used without further treatment for photocatalytic experiments.

2.6. Photocatalytic Degradations

A 300 W Osram lamp coupled with UV cut-off filter (λ > 420 nm) was used as light source for photocatalytic degradation experiments. In a typical photocatalytic experiment, 20 mg of photocatalyst was dispersed in 40 mL of the pollutant aqueous solution (Orange II or tetracycline hydrochloride, 10 mg/L) and the mixture was stirred in the dark for 60 min to reach the adsorption-desorption equilibrium. Next, visible light was turned on and at regular irradiation time intervals, 2 mL of the dispersion were withdrawn, centrifuged for 5 min at 15,000 rpm and analyzed by UV-visible absorption to monitor the degradation of the pollutant (485 nm for Orange II and 357 nm for tetracycline).

Scavenging experiments were conducted using the same synthetic protocol except that *tert*-butanol (*t*-BuOH), *p*-benzoquinone (*p*-BQ), ammonium oxalate (AO), sodium azide (NaN_3) and dimethylsulfoxide (DMSO) were added to the aqueous dispersions before turning on light.

2.7. Photocatalytic H_2 Production

For photocatalytic H_2 production, the surface of nanocomposites was decorated with NiS nanoparticles using $Ni(NO_3)_2$ and Na_2S as the precursors for NiS. In a typical experiment, 400 mg of the g-CN/TiO_2 (3:1) catalyst was dispersed in 45 mL of deionized water and 1.3 mL of a 0.05 M $Ni(NO_3)_2$ was added. The mixture was stirred for 20 min to absorb Ni^{2+} ions at the surface of the g-CN/TiO_2 (3:1) composite. Next, 1.5 mL of a 0.05 M Na_2S solution was added to the solution to form NiS. The obtained g-CN/TiO_2 (3:1)/NiS composite contains ca. 1.5 wt.% NiS and is noted g-CN/TiO_2 (3:1)/1.5%NiS. The association of NiS with the other g-CN/TiO_2 photocatalysts was conducted using the same synthetic protocol.

The photocatalytic hydrogen production was conducted in an outer irradiation type quartz reactor using a 300 W Xe lamp as the light source. A circulation of water with an external cooling coil was used to maintain the temperature of the dispersion at 25 °C. In order to remove dissolved oxygen, the dispersion was first bubbled with nitrogen for 60 min before light irradiation. The reactor was connected to a pure nitrogen gas flow (100 mL min^{-1}) used to displace hydrogen from the photoreactor toward the micro gas chromatograph (Varian 490-GC). In a typical experiment, 25 mg of photocatalyst was dispersed

in 50 mL aqueous solution containing 10 vol.% of glycerol used as sacrificial substrate and the mixture was stirred to ensure a uniform irradiation of the catalyst dispersion.

2.8. Apparent Quantum Efficiency (AQE)

The apparent quantum efficiency (AQE) was determined using the previously described experimental setup and with the Equation (1):

$$AQE = \frac{n \times \Delta G}{I} \times 100\% = \frac{n \times \Delta G}{W \times S \times t} \times 100\% \quad (1)$$

where n is the number of H_2 molecules evolved, ΔG = 237 kJmol^{-1} is the energy needed for one water molecule to entirely split into H_2 and O_2, W is the power of the lamp, S is the irradiated area, and t is the reaction time [33].

2.9. Photocatalyst Characterization

The morphology and the microstructure were investigated by scanning electron microscopy (SEM, Scanning Electron Microscope JSM-6490 LV, JEOL, Croissy, France) and transmission electron microscopy (TEM, Philips CM200 instrument operating at 200 kV, Philips, Suresnes, France). TEM images were acquired by placing a drop of the particles in water onto a gold grid.

X-ray powder diffraction (XRD) patterns were recorded using a Panalytical X'Pert Pro MPD diffractometer using Cu Kα radiation (λ = 0.15418 nm).

X-ray photoelectron spectroscopy (XPS) analyses were carried out on a Gammadata Scienta (Uppsala, Sweden) SES 200-2 spectrometer under ultra-high vacuum (P < 10^{-9} mbar).

Thermogravimetric analysis (TGA) was conducted under O_2 atmosphere using a TGA/DSC1 STAR equipment (Mettler-Toledo). Measurements were conducted from room temperature to 1000 °C at a heating rate of 10 °C min^{-1}.

The Brunauer–Emmett–Teller (BET) specific surface areas were measured with a Micromeritics ASAP 2420 instrument at liquid nitrogen temperature. Before analysis, the samples were out-gassed overnight in vacuum at 40 °C followed by 4 h out-gassing on the analysis port. The micropore volume was determined using the Barrett–Joyner–Halenda (BJH) method.

A Total Organic Carbon analyzer (Shimadzu TOC-VCSH, Marne-la-Vallée, France) was used to evaluate the amount of dissolved organic carbon before and after the photodegradation reactions.

Fourier transform infrared (FT-IR) spectra were recorded using a Brucker ALPHA spectrometer in the frequency range of 4000–450 cm^{-1}. UV-visible absorption spectra of liquid samples were measured using a Thermo Scientific Evolution 220 UV-visible spectrophotometer. The UV-visible diffuse reflectance spectra (DRS) were recorded on a Shimadzu 2600-2700 UV-visible spectrophotometer. Photoluminescence (PL) emission spectra were recorded at room temperature on a Horiba Fluoromax-4 Jobin Yvon spectrofluorimeter. Raman spectra were measured on a Horiba Scientific Xplora spectrometer using 532 nm wavelength incident YAG laser light.

The photoelectrochemical performance of the catalysts was evaluated in a three electrode cell using FTO glass coated with g-CN, TiO_2 or g-CN/TiO_2 composites with a surface area of 1 cm^2 as the working electrode, a Pt wire as the counter electrode and a saturated Ag/AgCl electrode as reference electrode. The electrolyte used was a 0.1 M Na_2SO_4 aqueous solution. The photocurrent densities were determined by measuring the current under 100 mW cm^{-2} light illumination provided by a 300 W Xe arc lamp equipped with an AM 1.5G filter. A SP150 BioLogic potentiostat was used to measure the photocurrent response at a constant potential of +0.30 V vs. the reference electrode.

3. Results

3.1. Photocatalysts Synthesis and Characterization

MIL-125(Ti) particles were produced from $Ti(On\text{-}Pr)_4$ and terephthalic acid in a DMF/MeOH mixture [39] and associated to exfoliated g-CN under sonication. Next, the g-CN/MIL-125(Ti) composites were calcined at 450 °C for 2 h to decompose MIL-125(Ti) into TiO_2 (Figure 1). A weight loss of ca. 50% was observed during the thermolysis of pure MIL-125(Ti). g-CN/MIL-125(Ti) composites with g-CN:MIL-125(Ti) weight ratios of 1:2, 2:2, 3:2, 4:2, and 8:2 were prepared to engineer g-CN/TiO_2 photocatalysts with g-CN:TiO_2 ratios of 1:1, 2:1, 3:1, 4:1, and 8:1, respectively.

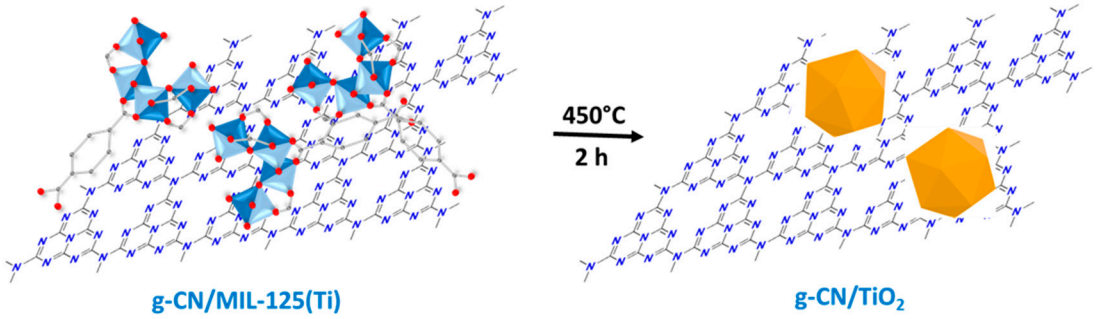

Figure 1. Schematic illustration of the preparation of the graphitic carbon nitride (g-CN)/TiO_2 photocatalysts from g-CN/MIL-125(Ti) composites.

The morphology, the structure and the composition of g-CN/MIL-125(Ti) and g-CN/TiO_2 composites were first investigated by SEM and TEM (Figure 2). After exfoliation by sonication, g-CN sheets have sizes varying from a few hundred of nanometers up to several micrometers and exhibit a crumpled layered morphology with a relatively smooth surface (Figure 2a). Using g-CN/MIL-125 (3:2) and g-CN/TiO_2 (3:1) samples as representatives, MIL-125(Ti) and TiO_2 particles are bound to g-CN sheets and uniformly distributed at their surface as indicated by SEM, TEM, TEM-associated EDS analyses and by the corresponding elemental mappings (Figure 2a–d, Figures S1 and S2). A marked exfoliation of g-CN can also be observed by SEM during the thermolysis of MIL-125(Ti) particles, which will be confirmed by BET specific surface measurements (*vide infra*). The SEM images show that MIL-125(Ti) particles decompose into TiO_2 particles with an average diameter of ca. 400 nm (Figure 2a,b) but TEM analyses demonstrate that TiO_2 is actually made up of clusters composed of TiO_2 nanoparticles with an average size of 12 ± 6 nm (Figure 2e). The HR-TEM image of these TiO_2 nanocrystals shows a lattice spacing of 0.35 nm, which corresponds to the (101) plane of anatase TiO_2 (Figure 2f).

The FT-IR spectrum of MIL-125(Ti) exhibits the typical vibrational bands between 1715 and 1300 cm^{-1} corresponding to the C=C and C-H bonds of the aromatic ring and to the asymmetric (1648 cm^{-1}) and symmetric (1386 cm^{-1}) stretching vibrations of the carboxylate functions (Figure 3a). The signals observed at 807, 739, and 657 cm^{-1} can be assigned to Ti-O-Ti-O vibrations [49]. For pure g-CN, the peaks located from 1658 to 1236 cm^{-1} correspond to the stretching modes of the carbon-nitrogen (C=N and C-N) bonds, while the sharp peak located at 806 cm^{-1} can be attributed to the out-of-plane breathing vibration of the s-triazine units [15,16,50]. The broad absorption bands at 3235 and 3154 cm^{-1} correspond to the stretching modes of NH_2 and NH functions. All these signals can be observed in the FT-IR spectra of g-CN/MIL-125(Ti) composites, indicating the successful deposition of MIL-125(Ti) at the surface of g-CN. Pure TiO_2 generated by the thermal decomposition of MIL-125 only exhibits a strong signal at 410 cm^{-1} corresponding to the vibration mode of Ti-O-Ti bonds in TiO_2 (Figure 3b) [51]. No signals of organics could be observed indicating that MIL-125 was efficiently decomposed into TiO_2 by heating at 450 °C for 2 h. The shift observed for the Ti-O bond from 412 to

460 cm^{-1} when increasing the g-CN:TiO_2 ratio from 1:1 to 8:1 suggests a strong interaction between TiO_2 and g-CN, which should favor the photocatalytic activity of these materials.

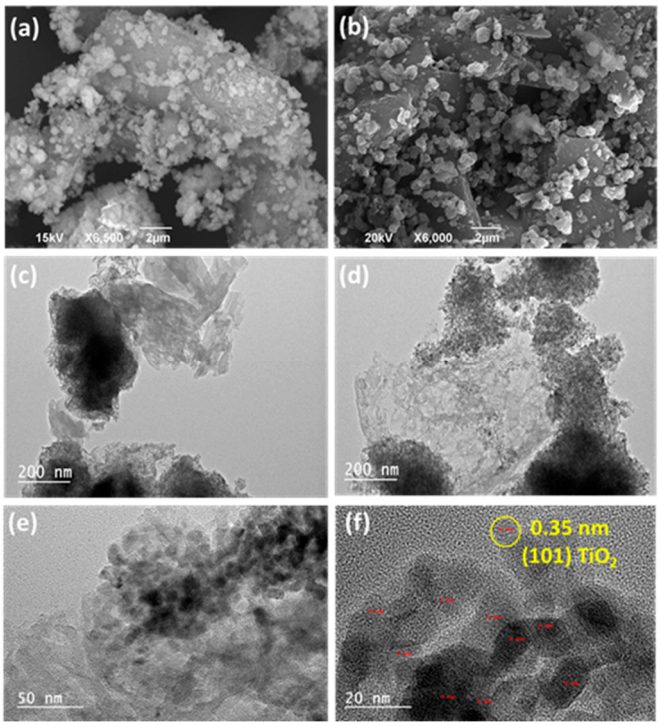

Figure 2. Scanning electron microscopy (SEM) images of (**a**) g-CN/MIL-125 (3:2) and (**b**) g-CN/TiO_2 (3:1), transmission electron microscopy (TEM) images of (**c**) g-CN/MIL-125 (3:1), and (**d**–**f**) g-CN/TiO_2 (3:1) composites.

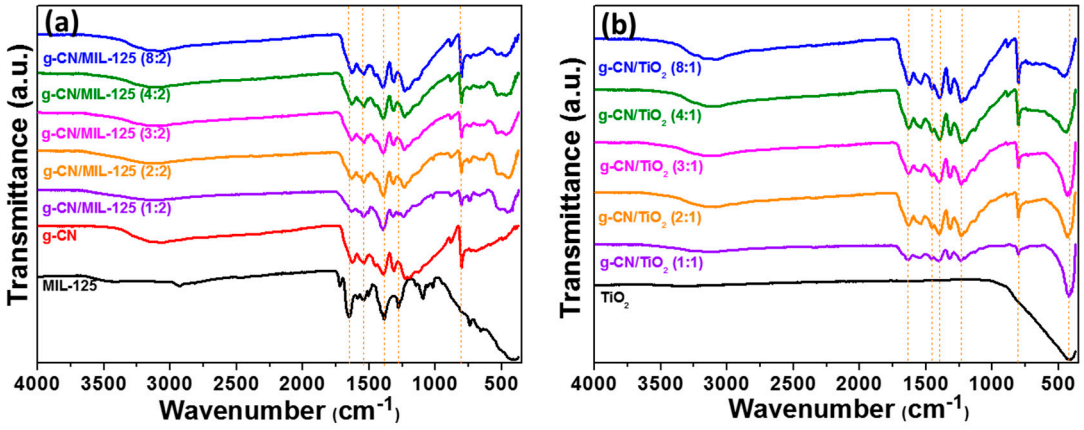

Figure 3. Fourier transform infrared (FT-IR) spectra of (**a**) MIL-125(Ti), g-CN, and of g-CN/MIL-125(Ti) composites and (**b**) TiO_2 and g-CN/TiO_2 composites.

XRD and Raman spectroscopy were used to analyse the structure of g-CN/TiO_2 composites. As previously observed after the pyrolysis of MIL-125(Ti) at a relatively mild temperature, the pure anatase phase of TiO_2 is formed (Figure 4a) [42,44]. The peaks at 2θ values of 25.35, 36.83, 37.93, 38.72, 48.16, 54.19, 55.16, and 62.75° belong to the (101), (103), (004), (112), (200), (105), (211), and (204) lattice planes of anatase (JCPDS No 21-1272). For g-CN, the diffraction peaks located at 13.03° and 27.51° are related to the (100) interplanar structural packing (repeated s-triazine units) and to the (002) interlayer stacking structure [15,16]. Compared to bulk g-CN, a slight decrease of the cristallite size from 7.4 to 6.9 nm (Figure S3) and a slight shift to higher angles of the (002) peak (Figure S4) were observed

for exfoliated g-CN. The intensity of the g-CN related peaks increases with the g-CN content of the nanocomposites. Moreover, a shift of the (002) reflection from 27.51° to 27.66° is observed after the thermolysis of MIL-125(Ti), which confirms the strong interaction of TiO_2 nanoparticles with g-CN sheets. The Raman spectrum of pure TiO_2 shows peaks at 395, 518, and 639 cm^{-1} corresponding to the *B1g*, *A1g* + *B1g* and *Eg* modes of anatase TiO_2, respectively (Figure 4b) [52]. Despite the modest resolution of the g-CN Raman spectrum using the 532 nm laser, three strong peaks corresponding to the vibration of s-triazine units can be observed at 472, 705, and 1234 cm^{-1} [53]. The Raman signals of TiO_2 and g-CN can all be observed in g-CN/TiO_2 composites, further confirming the structure of these materials.

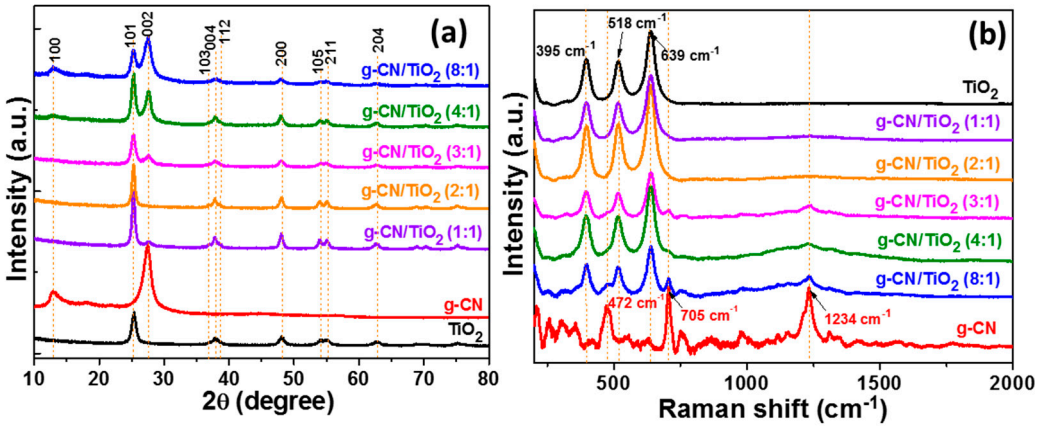

Figure 4. (**a**) X-ray powder diffraction (XRD) patterns and (**b**) Raman spectra of TiO_2, g-CN, and g-CN/TiO_2 composites.

The actual weight ratio of TiO_2 in g-CN/TiO_2 composites and the thermal stability of these photocatalysts were determined by TGA. The TGA profiles of the g-CN/TiO_2 photocatalysts recorded in air atmosphere with a heating rate of 10 °C min^{-1} are given in Figure 5. The weak weight loss (ca. 2%) observed below 100 °C originates from the removal of water molecules adsorbed at the surface of the catalysts. As can be seen from Figure 5, g-CN starts to decompose at ca. 550 °C into CO_2 and NO_2. A sharp weight loss is observed at ca. 580 °C for all composites. The content in g-CN was determined from the remaining TiO_2 weight and was found to be significantly lower than the theoretical ratio (Table 1). The relative content in g-CN is the lowest for composites with a high loading in TiO_2 (g-CN/TiO_2 ratios of 1:1 and 2:1), suggesting that TiO_2 promotes the thermal decomposition of g-CN.

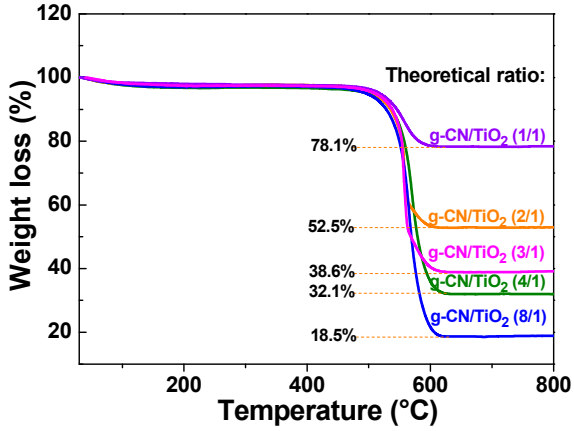

Figure 5. Thermogravimetric curves of g-CN/TiO_2 composites.

Table 1. Theoretical and actual g-CN:TiO_2 ratios determined by thermogravimetric analysis (TGA) analyses.

Theoretical g-CN:TiO_2 Ratio	1:1	2:1	3:1	4:1	8:1
Actual g-CN:TiO_2 Ratio	0.28:1	0.91:1	1.59:1	2.12:1	4.41:1

X-ray photoelectron spectroscopy (XPS) was used to investigate the composition and the surface chemical states of C, N, Ti and O elements present in the g-CN/TiO_2 (3:1) composite (Figure S5). The major signal in the XPS high resolution C 1s spectrum is located at 288.08 eV and can be assigned to sp^2-hybridized C atoms in nitrogen heterocycles (Figure S6a). The weaker signal observed at 284.93 eV originates from sp^2-hybridized C-C bonds [54,55]. The N 1s spectrum can be deconvoluted into three peaks at 401.15 eV (N-N bonding structure), 400.09 eV (tertiary nitrogen atoms, N-$(C)_3$) and 398.54 eV (sp^2-hybridized N in triazine rings, C-N=C) (Figure S6b) [55]. The weak signal observed at 404.51 eV can be attributed to charging effects. For Ti 2p, two signals located at 458.87 eV and 464.62 eV corresponding to Ti $2p_{3/2}$ and Ti $2p_{1/2}$, respectively, can be observed (Figure S6c). The doublet splitting energy of Ti 2p is of 5.75 eV, which confirms that Ti is in the +4 oxidation state [56]. Finally, the O 1s spectrum can be deconvoluted into two peaks at 530.11 and 532.30 eV corresponding to lattice oxygen atoms (Ti-O bonds) and to carbonate species adsorbed at the surface of the photocatalyst, respectively (Figure S6d).

The BET specific surface areas and the porosities of g-CN, TiO_2, and g-CN/TiO_2 photocatalysts were investigated by nitrogen adsorption–desorption experiments. Figure 6a shows that all materials exhibit isotherms of type IV according to the Brunauer–Deming–Deming–Teller (BDDT) classification, indicating the presence of mesopores. The hysteresis loops observed at high relative pressure ($P/P_0 > 0.8$) suggest the presence of slit-like pores, which is consistent with the morphology of the photocatalysts determined by SEM and TEM (Figure 2). Pure g-CN exhibits a low BET specific surface area (9.8 m^2g^{-1}), which is in accordance with previous reports (Table 2) [15,16]. The BET specific surface area of pure TiO_2 is significantly higher (56.3 m^2g^{-1}), indicating that the textural properties of MIL-125(Ti) were partly transferred to TiO_2 after the calcination step. The BET specific surface areas of g-CN/TiO_2 composites increase with the content in g-CN until the g-CN:TiO_2 ratio of 2:1 and then decrease, which suggests than an optimal amount of MIL-125(Ti) favours the exfoliation of g-CN during the heating at 450 °C and thus the increase of the specific surface area. This may originate from the production of gases like CO_2 during the thermolysis of MIL-125(Ti) that generate more larger pores that allow to increase the BET specific surface area. The gradual decrease of S_{BET} when increasing the g-CN:TiO_2 ratio from 3:1 to 8:1 may originate from a pore blocking of TiO_2 by g-CN. The S_{BET} values measured for g-CN/TiO_2 composites prepared via annealing of $Ti(On\text{-}Bu)_4$ in the presence of g-CN or by calcination of melamine in the presence of TiO_2 crystals typically range from 34 to 77 m^2g^{-1} [19,22,23,26,28]. The specific surface areas of g-CN/TiO_2 (2:1 and 3:1) photocatalysts are significantly higher (ca. 102 and 86 m^2g^{-1}) suggesting that during the calcination step, g-CN:MIL-125(Ti) ratios of 2:2 and 3:2 are optimal to simultaneously exfoliate g-CN and to generate porous TiO_2. Finally, the pore volumes and pore sizes were determined according to the Barrett–Joyner–Halenda (BJH) method (Figure 6b, Table 2). As previously, the higher pore volume values were obtained for the g-CN/TiO_2 2:1 and 3:1 materials (up to 0.29 cm^3g^{-1}). The large size of these pores further confirms the presence of mesopores. The high specific surface areas of g-CN/TiO_2 2:1 and 3:1 materials associated to their mesoporosity will provide more surface-active sites and thus should improve their photocatalytic performance.

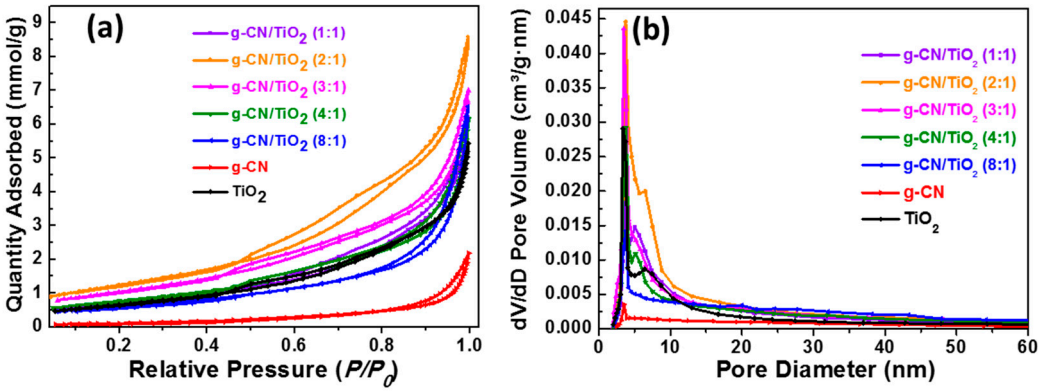

Figure 6. (**a**) Nitrogen adsorption-desorption isotherms of TiO_2, g-CN, and g-CN/TiO_2 photocatalysts and (**b**) the corresponding pore-size distributions.

Table 2. Brunauer–Emmett–Teller (BET) specific surface areas, pore volumes and pore sizes of g-CN, TiO_2, and g-CN/TiO_2 composites.

Sample	BET (m^2g^{-1})	Pore Volume (cm^3g^{-1})	Pore Size (nm)
g-CN	9.8 ± 0.2	0.07	17.75
TiO_2	56.3 ± 0.4	0.18	10.19
g-CN/TiO_2 (1:1)	59.8 ± 0.3	0.20	11.15
g-CN/TiO_2 (2:1)	102.2 ± 0.4	0.29	9.42
g-CN/TiO_2 (3:1)	86.2 ± 0.3	0.23	9.53
g-CN/TiO_2 (4:1)	63.8 ± 0.1	0.20	11.19
g-CN/TiO_2 (8:1)	48.8 ± 0.2	0.21	16.05

UV-visible absorption spectra of TiO_2, g-CN, and g-CN/TiO_2 composites are shown in Figure 7a and the bandgap energy of the materials were determined using the relation $\alpha h\upsilon = A(h\upsilon - Eg)^2$ where α, h, υ, A, and Eg at the absorption coefficient, the Plank's constant, the frequency of light, a constant, and the bandgap energy, respectively. Pure anatase TiO_2 and g-CN exhibit bandgap energies of 3.02 and 2.70 eV, respectively, values in good accordance with those described in the literature (Figure 7b) [15,16,57]. With the increase of the g-CN loading in the photocatalysts, the UV-visible absorption in the 400–470 nm range increases and simultaneously the bandgap energy decreases from 3.02 to 2.73 eV. This extension of TiO_2 absorption should improve its photocatalytic performance in the visible range.

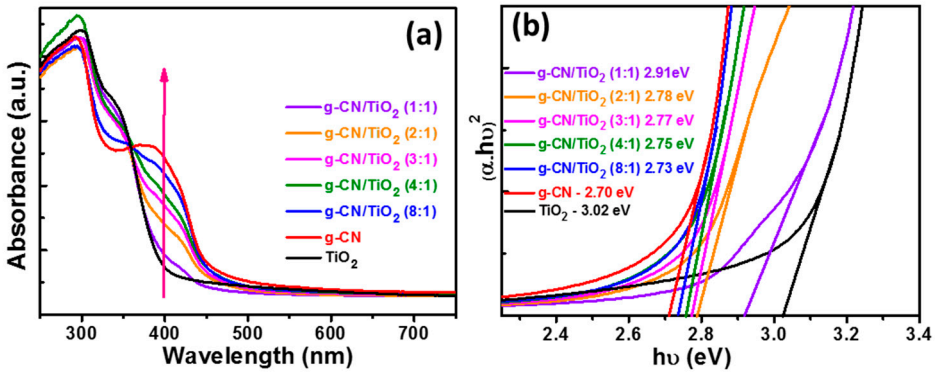

Figure 7. (**a**) UV-visible absorption spectra of TiO_2, g-CN, and g-CN/TiO_2 composites and (**b**) plots of $(\alpha h\gamma)^2$ vs $h\gamma$ used to determine the energy bandgap of the photocatalysts.

3.2. Photodegradation of Pollutants under Visible Light Irradiation

First, the surface charges of g-CN and of the g-CN/TiO_2 (3:1) catalysts in water were determined. For pure g-CN, the point of zero charge (pzc) was determined to be 4.23, value in good agreement with previous reports (Figure S7) [58]. As the pzc of pure TiO_2 is usually between 3 and 4 [59], the pzc of the g-CN/TiO_2 composite slightly decreases to 3.70 after deposition of TiO_2 at the surface of g-CN sheets. These results show that the g-CN/TiO_2 photocatalyst exhibits a positive charge at neutral pH and should associate via electrostatic interactions with negatively-charged pollutants in aqueous solution.

In a first set of experiments, the photocatalytic activity of g-CN/TiO_2 materials was evaluated in the bleaching of the anionic diazo Orange II dye (concentration of 10 mgL^{-1}) under visible light irradiation (intensity of 15 $mWcm^{-2}$). Figure 8a depicts the variation of the relative concentration (C/C_0) of Orange II vs irradiation time with respect to the changes of the dye absorption at 485 nm. The g-CN/TiO_2 (3:1) composite exhibits the highest degradation efficiency for Orange II (ca. 95% bleaching after 180 min irradiation) while control experiments using TiO_2 or g-CN showed significantly lower degradation efficiencies (22 and 50%, respectively) after the same illumination period. The photocatalytic activity increases with the increase of the g-CN/TiO_2 ratio until 3:1 and then slightly decreases for composites prepared with g-CN:TiO_2 ratios of 4:1 and 8:1, which suggest that the charge-carrier transfer efficiency is the highest when using the 3:1 g-CN:TiO_2 ratio. The decrease of the photocatalytic efficiency for g-CN/TiO_2 4:1 and 8:1 composites is likely related to the decrease of their specific surface area as shown in Table 2 and to the increased charge carrier recombination (see below). Figure S8 shows the time dependent changes in the UV-visible absorption spectrum of Orange II during its photodegradation by the g-CN/TiO_2 (3:1) catalyst. In the meantime, the orange color of the solution gradually disappeared, indicating that the structure of the dye was decomposed. The total organic carbon (TOC) decreased from 5.48 to 1.13 gL^{-1} after 180 min irradiation, which confirms the efficient mineralization of the dye. The first-order kinetics of Orange II degradation over the different photocatalysts are plotted in Figure S9. The apparent first-order rate constants k are 0.0033, 0.0058, 0.0156, 0.0137, and 0.0106 min^{-1} for g-CN/TiO_2 catalysts prepared with g-CN:TiO_2 ratios of 1:1, 2:1, 3:1, 4:1, and 8:1, respectively, further confirming that the g-CN/TiO_2 (3:1) composite exhibits the highest photocatalytic activity.

The g-CN/TiO_2 (3:1) photocatalyst was also successfully used for the degradation of tetracycline hydrochloride, an antibiotic commonly used in human and veterinary medicine [60] and which poses serious threats on various eco-systems due to its poor biodegradability [61]. The photocatalytic activity of the g-CN/TiO_2(3:1) composite was compared to that of pure TiO_2 and g-CN (Figure 8b). A marked absorption of tetracycline at the surface of g-CN/TiO_2 and TiO_2 catalysts (ca. 40 and 20%, respectively) was observed. Although tetracycline exists in its zwitterionic form at neutral pH [62], these results suggest that the enolate form of tetracycline strongly binds to the positively-charged surface of TiO_2 and g-CN/TiO_2 catalysts. The photocatalytic activity of the g-CN/TiO_2 composite under visible light irradiation is significantly higher than that of TiO_2 and g-CN, further confirming that the association of g-CN and TiO_2 improves the separation of electron-hole pairs. The apparent first-order rate constant k determined for TiO_2, g-CN, and g-CN/TiO_2 photocatalysts are 0.0035, 0.0078, and 0.0093 min^{-1}, respectively, and confirm that the kinetic of degradation is the highest for the g-CN/TiO_2 (3:1) composite (Figure S10). As can also be seen from Figure S11, almost 95% of tetracycline is decomposed after 180 min visible light irradiation. Moreover, the TOC value decreased from 5.48 to 1.63 g L^{-1}, further demonstrating that the g-CN/TiO_2 (3:1) catalyst is of high interest for environmental applications. The performances of the g-CN/TiO_2 (3:1) composite are higher than those of g-CN based catalysts recently developed for the degradation of TC (P- and S-doped g-CN, C-doped g-CN, or WO_3/g-CN/Bi_2O_3, 70–85% degradation after ca. 1 h using a light intensity of 100 $mWcm^{-2}$) when considering that a much lower intensity irradiation was used in our experiments (25 $mWcm^{-2}$) [63–65].

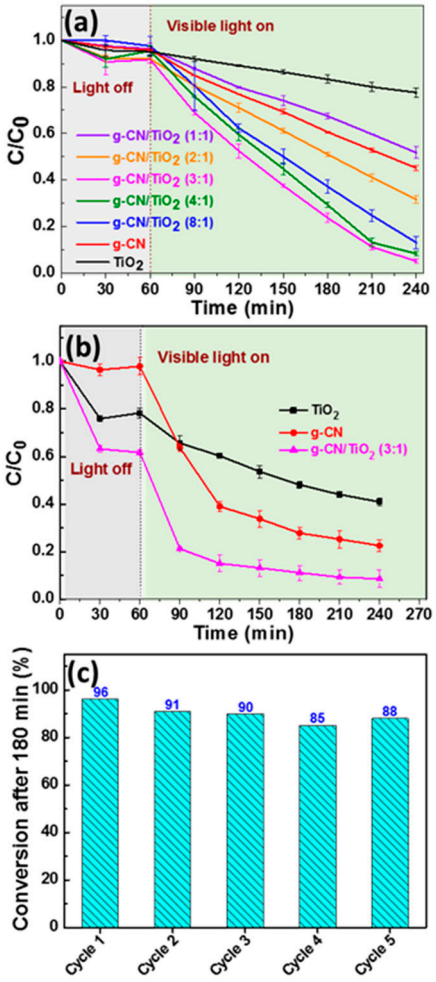

Figure 8. Photocatalytic degradation profiles of (**a**) Orange II and (**b**) tetracycline over TiO_2, g-CN, and g-CN/TiO_2 catalysts under visible light irradiation, and (**c**) photodegradation stability of Orange II using the g-CN/TiO_2 (3:1) catalyst.

The photocatalytic stability of the g-CN/TiO_2 (3:1) composite was evaluated by five consecutive tests using Orange II as model pollutant (Figure 8c). A slight decrease of the dye degradation efficiency is observed after the first cycle (91%) but after the catalyst activity remains almost stable (88% after the fifth reuse), which indicates that the g-CN/TiO_2 (3:1) composite shows a good stability as a photocatalyst. In addition, XRD analyses indicate that the crystallinity of the material is not affected by the reuses (Figure S12).

3.3. Active Species Involved in the Photodegradation, Photoelectrochemical Measurements, and Mechanism

To identify the active species responsible for the degradation of Orange II, trapping experiments were conducted using *tert*-butanol (*t*-BuOH), *p*-benzoquinone (*p*-BQ), ammonium oxalate (AO), sodium azide (NaN_3), and DMSO as hydroxyl radicals ($^{\bullet}OH$), superoxide radicals ($O_2^{\bullet-}$), holes (h^+), singlet oxygen ($^1O_2$), and electron (e^-) scavengers, respectively [15,16]. Figure 9a shows the influence of these scavengers on the photocatalytic performance of the g-CN/TiO_2 (3:1) composite after 180 min irradiation. Weak decreases of the Orange II photodegradations were observed when adding *t*-BuOH and DMSO (88.5 and 83.3%, respectively) indicating that $^{\bullet}OH$ radicals and electrons only play a minor role in the mechanism. The photodegradation efficiencies more significantly declined upon addition of AO and NaN_3 (67 and 43.7%, respectively) indicating that h^+ and $^1O_2$ are involved in the degradation.

Finally, $O_2^{\bullet-}$ radicals play the key role in the photodegradation as the most deleterious effect was observed using *p*-BQ (7.5% after 180 min irradiation).

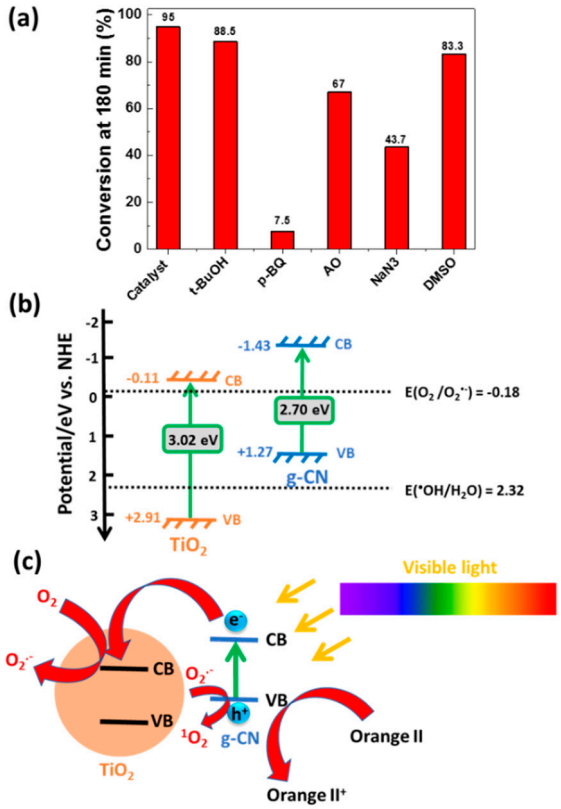

Figure 9. (**a**) Photodegradation of Orange II under visible light irradiation using the g-CN/TiO_2 catalyst in the presence of reactive species trapping compounds, (**b**) band structure of the g-CN/TiO_2 photocatalyst, and (**c**) schematic illustration of the delocalization of charge carriers and of the formation of reactive species involved in the photodegradation of Orange II.

The band edge position of the valence band (VB) of TiO_2 at the point of zero charge can be calculated using the empirical Equation (2):

$$E_{CB} = \chi - E^e - 0.5\,Eg \quad (2)$$

where E_{CB} is the CB potential, χ is the absolute electronegativity of TiO_2 (5.90 eV), E^e is the energy of free electrons on the hydrogen scale (ca. 4.5 eV), and Eg is the bandgap energy (3.02 eV) [66]. The band edge positions of the VB and of the CB of TiO_2 nanoparticles were estimated to be +2.91 and −0.11 eV, respectively. For g-CN with a χ value of 4.42 eV, E_{CB} and E_{VB} values were determined to be −1.43 and +1.27 eV, respectively. A diagram showing the band structure of g-CN/TiO_2 nanocomposite is presented in Figure 9b along with the redox potentials of the reference reactions.

On the basis of these data, a scheme for the photogenerated electron/hole transfer steps under visible light irradiation at the interface of the g-CN/TiO_2 catalyst can be proposed (Figure 9b,c). Under visible light irradiation (λ > 420 nm), only g-CN is able to absorb photons, which results in the transfer of electrons from the VB to the CB of TiO_2. Due to the electrostatic field at the junction, photoexcited electrons can easily transfer to the CB while holes remain in g-CN, thereby hindering the charge carriers recombination and increasing the lifetimes of photogenerated electrons and holes. Then, separated electrons and holes can initiate reduction and oxidation reactions with O_2 and H_2O molecules adsorbed on the catalyst surface. The VB potential of g-CN (+1.27 eV) is higher than that of the $^{\bullet}OH/H_2O$ couple (+2.32 eV) and holes in the VB g-CN cannot react with H_2O to generate $^{\bullet}OH$

radicals. However, these holes can oxidize Orange II into Orange II^{+}. In the meantime, electrons accumulated in the CB of TiO_2 can easily react with O_2 to generate $O_2^{\bullet-}$ radicals. These radicals can directly oxidize the dye or transfer electrons to the holes in the VB of g-CN to give $^1O_2$. These data are in good accordance with scavenging results described in Figure 9a where $O_2^{\bullet-}$, holes and $^1O_2$ were demonstrated to play the major role in the photodegradation mechanism.

To support the enhanced photocatalytic performance of the g-CN/TiO_2 (3:1) composite under visible light irradiation, the recombination process of photogenerated electron-hole pairs in g-CN, TiO_2 and g-CN/TiO_2 composites was first investigated by PL spectroscopy. Upon excitation at 350 nm, g-CN exhibits a strong PL emission with the main signal located at 439 nm while TiO_2 is non-fluorescent (Figure 10a). The shape of the PL peak for g-CN/TiO_2 composites is similar to that of g-CN but its intensity is weaker indicating that the electron-hole pair's recombination is hampered. There is no correlation between the g-CN loading in g-CN/TiO_2 composites and the PL intensity gradually decreases when increasing the g-CN:TiO_2 ratio from 1:1 to 3:1 before re-increasing for the 4:1 and 8:1 ratios. The separation of electron-hole pairs is the most efficient in the g-CN/TiO_2 (3:1) material, which is consistent with photocatalytic results.

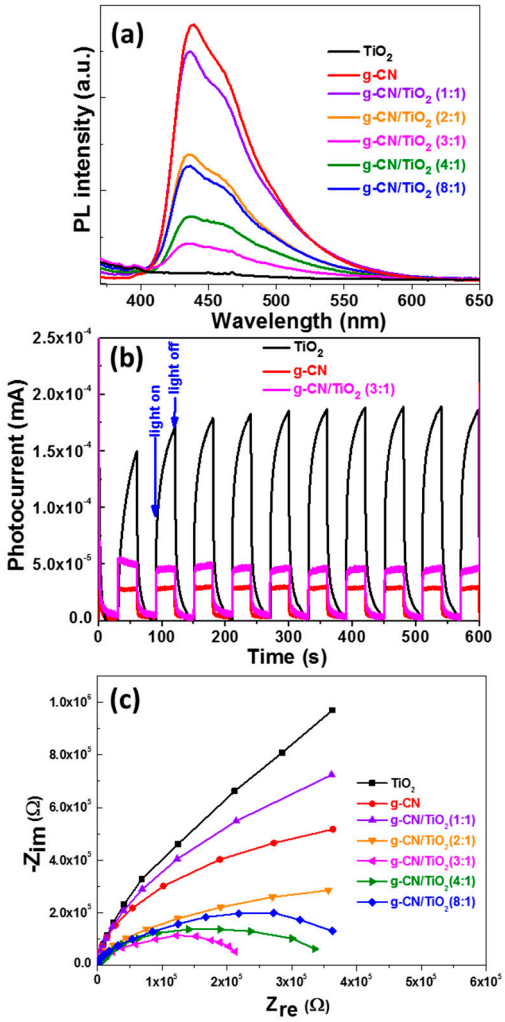

Figure 10. (**a**) Room temperature photoluminescence (PL) emission spectra of TiO_2, g-CN, and g-CN/TiO_2 materials (λ_{ex} = 350 nm), (**b**) Photocurrent responses of TiO_2, g-CN, and g-CN/TiO_2 (3:1) composite under visible light irradiation and (**c**) EIS Nyquist plots of TiO_2, g-CN, and g-CN/TiO_2 materials.

The electronic interactions in the various g-CN/TiO_2 photocatalysts were also studied by measuring the photocurrent responses and by using electrochemical impedance spectroscopy (EIS). Figure 10b shows the I–t curves of g-CN, TiO_2, and g-CN/TiO_2 (3:1) materials during ten on–off cycles of visible light irradiation. The photocurrent quickly increases when light is turned on and decreases to zero when the light is turned off, indicating that the materials respond to light with a good reproducibility. An improved charge carrier separation efficiency and a fastest charge transfer through the electrode interface are observed for the g-CN/TiO_2 (3:1) composite as the photocurrent response is ca. 1.8-fold higher than that of g-CN. Due to its bandgap energy of 3.02 eV (410 nm), pure TiO_2 responds to visible light irradiation. However, the photocurrent continuously increases during the illumination and does not reach a steady state contrary to g-CN and to the g-CN/TiO_2 (3:1) composite. A similar behavior was previously observed and may originate either from photo-excited states exhibiting a short lifetime and/or from a better contact between TiO_2 and the electrode during photoelectrochemical measurements [19].

The transfer resistance of electrons on the electrode surface plays also a key role on the electron transfer efficiency. The Nyquist plots of the EIS for TiO_2, g-CN, and g-CN/TiO_2 photocatalysts are shown in Figure 10c. The smallest diameter of the semi-circular Nyquist plots is observed for the g-CN/TiO_2 (3:1) composite which further confirms that the electron transfer is the fastest in this material.

3.4. Hydrogen Photoproduction

The hydrogen production activity of g-CN/TiO_2/NiS catalysts was evaluated using a 300 W Xenon lamp as light source and an aqueous solution containing 10 vol.% glycerol as sacrificial substrate. Pure TiO_2 and g-CN were used as references in these experiments. The efficient and cheap NiS co-catalyst which has shown its effectiveness for H_2 photoproduction using g-CN and TiO_2 was used instead of noble metals like Pt or Pd [67,68]. After deposition of NiS at the surface of g-CN/TiO_2 (4:1), (3:1), and (2:1) composites, photogenerated electrons likely transfer from the g-CN/TiO_2 photocatalyst to the valence band of the NiS semiconductor (Z-scheme transfer) which promotes H_2 evolution according to Equations (3) and (4):

$$NiS + e^- + H^+ \rightarrow HNiS \quad (3)$$

$$HNiS + e^- + H^+ \rightarrow NiS + H_2 \quad (4)$$

Meanwhile, electrons are reinjected in the g-CN/TiO_2 photocatalyst via the oxidation of the sacrificial substrate.

Control experiments show that H_2 is not produced in the absence of the photocatalyst or light irradiation. As can be seen from Figure 11, H_2 is produced immediately after turning on light and the hydrogen evolution rate (HER) remains almost stable along the 3 h of irradiation. The highest HER values were obtained for the g-CN/TiO_2 (3:1) catalyst (1330, 1256, and 1223 $\mu molh^{-1}g^{-1}$ after 1, 2, and 3 h of irradiation, respectively). These HERs are ca. 1.65- and 5.8-times higher than those measured for TiO_2 and g-CN. The apparent quantum efficiency (AQE) of the g-CN/TiO_2 (3:1) photocatalyst is of 0.22%, value 1.7-fold and 5.8-fold higher than those determined for pure TiO_2 and g-CN, respectively. These results further demonstrate that the heterojunction constructed between TiO_2 and g-CN combined to the high specific surface of the catalyst contribute to the enhancement of photogenerated electron transfer and thus to the photocatalytic activity. Finally, the photocatalytic activity for H_2 production is at least 2.6-times higher than that of binary g-CN/TiO_2 catalyst recently described in the literature (the highest HER values vary from 446 to 500 $\mu molh^{-1}g^{-1}$) [18,25,32,33]. Noteworthy is also that some higher values were reported (up to 8931 $\mu molh^{-1}g^{-1}$) but using Pt as co-catalyst [22].

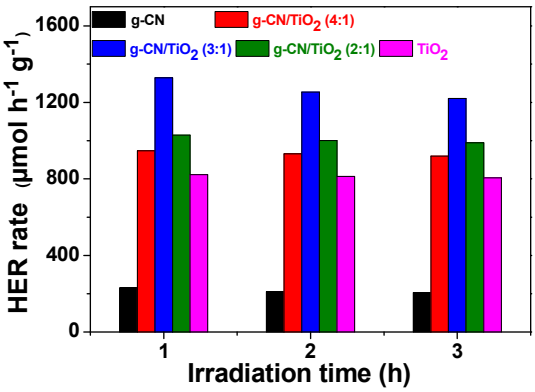

Figure 11. Photocatalytic hydrogen production rates after 1, 2, and 3 h illumination of g-CN, TiO_2, and g-CN/TiO_2 catalysts associated to the NiS cocatalyst (1.5 wt.%) using a 300 W Xe lamp as irradiation source and water containing 10 vol.% glycerol as sacrificial substrate.

4. Conclusions

Photocatalysts associating TiO_2 nanoparticles with an average size of ca. 12 nm and g-CN sheets were efficiently prepared by thermolysis of MIL-125(Ti) particles in the presence of g-CN. The high specific surface area of MIL-125(Ti) is transferred to TiO_2 nanoparticles and g-CN/TiO_2 composites exhibiting specific surface area up to 102 m^2g^{-1} could be engineered using the synthetic protocol developed in this work. The g-CN/TiO_2 (3:1) composite was demonstrated to exhibit the highest photocatalytic activity both for the degradation of pollutants like Orange II or tetracycline and for hydrogen production (HER of 1330 $\mu molh^{-1}g^{-1}$ after 1 h irradiation without using Pt as co-catalyst). The close interfacial connection between TiO_2 and g-CN allows the efficient charge carriers separation with photo-excited electrons transferred from g-CN to TiO_2 while holes remain in g-CN. The design of heterostructured materials using the thermal decomposition of metal organic frameworks to generate porous metal oxide like TiO_2 was demonstrated to be an efficient strategy to improve the solar utilization for photocatalytic applications.

Supplementary Materials: The following are available online at http://www.mdpi.com/2079-4991/10/7/1387/s1, Figure S1: (a) SEM image, (b) EDX analysis, and (c–f) EDX mapping of the g-CN/MIL-125(Ti) (3:2) composite. Figure S2: (a) SEM image, (b) EDX analysis, and (c-g) EDX mapping of the g-CN/TiO_2 (3:1) composite. Figure S3. XRD analysis of the (002) peak for (a) bulk g-CN and (b) exfoliated g-CN using the DIFFRAC.EVA software from Bruker. Figure S4. XRD patterns of bulk and exfoliated g-CN. Figure S5: XPS survey spectrum of the g-CN/TiO_2 (3:1) photocatalyst. Figure S6: High resolution XPS spectra of (a) C 1s, (b) N 1s, (c) Ti 2p, and (d) O 1s for the g-CN/TiO2 (3:1) photocatalyst. Figure S7: Zeta potentials of g-CN and g-CN/TiO_2 (3:1) photocatalysts as a function of pH. Figure S8: UV-vis spectrum changes of Orange II during its photodegradation by the g-CN/TiO_2 (3:1) composite. Figure S9: Pseudo-first-order kinetics fitted curves of Orange II degradation over TiO_2, g-CN, and g-CN/TiO_2 composites under visible light irradiation. Figure S10: Pseudo-first-order kinetics fitted curves of tetracycline degradation over TiO_2, g-CN, and the g-CN/TiO_2 (3:1) composite under visible light irradiation. Figure S11: UV-vis spectrum changes of tetracycline during its photodegradation by the g-CN/TiO_2 (3:1) composite. Figure S12: XRD patterns of the g-CN/TiO_2 (3:1) catalyst after synthesis (black line) and after 5 reuses for the degradation of the Orange II dye (red line).

Author Contributions: Conceptualization, R.S. and B.U.; methodology, R.S., B.T., and B.C.; validation, B.T., B.C., T.G., L.B., E.G. and R.S.; investigation, B.T., B.C., L.B., T.G., E.G., and G.M.; writing—original draft preparation, B.T. and B.C.; writing—review and editing, B.T., B.C., and R.S.; project administration, R.S. and B.U.; funding acquisition, B.U. and R.S. All authors have read and agreed to the published version of the manuscript.

Funding: The authors thank the Bolashak International Scholarship of JSC "Center for International Programs" for financial support.

Conflicts of Interest: The authors declare no conflict of interest.

References

1. Fu, J.; Yu, J.; Jiang, C.; Cheng, B. g-C_3N_4-Based Heterostructured Photocatalysts. *Adv. Energy Mater.* **2018**, *8*, 1701503. [CrossRef]
2. Li, H.; Zhou, Y.; Tu, W.; Ye, J.; Zou, Z. State-of-the-Art Progress in Diverse Heterostructured Photocatalysts toward Promoting Photocatalytic Performance. *Adv. Funct. Mater.* **2015**, *25*, 998–1013. [CrossRef]
3. Wang, Y.; Wang, Q.; Zhan, X.; Wang, F.; Safdar, M.; He, J. Visible light driven type II heterostructures and their enhanced photocatalysis properties: A review. *Nanoscale* **2013**, *5*, 8326–8339. [CrossRef] [PubMed]
4. Zhang, P.; Lou, X.W. Design of Heterostructured Hollow Photocatalysts for Solar-to-Chemical Energy Conversion. *Adv. Mater.* **2019**, *31*, 1900281. [CrossRef] [PubMed]
5. Li, X.; Yu, J.; Low, J.; Fang, Y.; Xiao, J.; Chen, X. Engineering heterogeneous semiconductors for solar water splitting. *J. Mater. Chem. A* **2015**, *3*, 2485–2534. [CrossRef]
6. Shayegen, Z.; Lee, C.-S.; Haghighat, F. TiO_2 photocatalyst for removal of volatile organic compounds in gas phase–A review. *Chem. Eng. J.* **2018**, *334*, 2408–2439. [CrossRef]
7. Low, J.; Cheng, B.; Yu, J. Surface modification and enhanced photocatalytic CO_2 reduction performance of TiO_2: A review. *Appl. Surf. Sci.* **2017**, *392*, 658–686. [CrossRef]
8. Kumaravel, V.; Mathew, S.; Bartlett, J.; Pillai, S.C. Photocatalytic hydrogen production using metal doped TiO_2: A review of recent advances. *Appl. Catal. B Environ.* **2019**, *244*, 1021–1064. [CrossRef]
9. Ge, M.; Cai, J.; Iocozzia, J.; Cao, C.; Huang, J.; Zhang, X.; Shen, J.; Wang, S.; Zhang, S.; Zhang, K.-Q.; et al. A review of TiO_2 nanostructured catalysts for sustainable H_2 generation. *Int. J. Hydrog. Energy* **2017**, *42*, 8418–8449. [CrossRef]
10. Fagan, R.; McCormack, D.E.; Dionysiou, D.P.; Pillai, S.C. A review of solar and visible light active TiO_2 photocatalysis for treating bacteria, cyanotoxins and contaminants of emerging concern. *Mater. Sci. Semicond. Process.* **2016**, *42*, 2–14. [CrossRef]
11. Shwetharani, R.; Sakar, M.; Fernando, C.A.N.; Binas, V.; Balakrishna, R.G. Recent advances and strategies to tailor the energy levels, active sites and electron mobility in titania and its doped/composite analogues for hydrogen evolution in sunlight. *Catal. Sci. Technol.* **2019**, *9*, 12–49. [CrossRef]
12. Wen, J.; Xie, J.; Chen, X.; Li, X. A review on g-C_3N_4-based photocatalysts. *Appl. Surf. Sci.* **2017**, *391*, 72–123. [CrossRef]
13. Masih, D.; Ma, Y.; Rohani, S. Graphitic C_3N_4 based noble-metal-free photocatalyst systems: A review. *Appl. Catal. B Environ.* **2017**, *206*, 556–588. [CrossRef]
14. Zhang, S.; Gu, P.; Ma, R.; Luo, C.; Wen, T.; Zhao, G.; Cheng, W.; Wang, X. Recent developments in fabrication and structure regulation of visible-light-driven g-C_3N_4-based photocatalysts towards water purification: A critical review. *Catal. Today* **2019**, *335*, 65–77. [CrossRef]
15. Moussa, H.; Chouchene, B.; Gries, T.; Balan, L.; Mozet, K.; Medjahdi, G.; Schneider, R. Growth of ZnO Nanorods on Graphitic Carbon Nitride gCN Sheets for the Preparation of Photocatalysts with High Visible-Light Activity. *ChemCatChem* **2018**, *10*, 4973–4983. [CrossRef]
16. Ouedraogo, S.; Chouchene, B.; Desmarets, C.; Gries, T.; Balan, L.; Fournet, R.; Medjahdi, G.; Bayo, K.; Schneider, R. Copper octacarboxyphthalocyanine as sensitizer of graphitic carbon nitride for efficient dye degradation under visible light irradiation. *Appl. Catal. A Gen.* **2018**, *563*, 127–136. [CrossRef]
17. Obregon, S.; Colon, G. Improved H_2 production of Pt-TiO_2/g-C_3N_4-MnOx composites by an efficient handling of photogenerated charge pairs. *Appl. Catal. B Environ.* **2014**, *144*, 775–782. [CrossRef]
18. Elbanna, O.; Fujitsuka, M.; Majima, T. g-C_3N_4/TiO_2 Mesocrystals Composite for H_2 Evolution under Visible-Light Irradiation and Its Charge Carrier Dynamics. *ACS Appl. Mater. Interfaces* **2017**, *9*, 34844–34854. [CrossRef]
19. Troppova, I.; Sihar, M.; Rehi, M.; Ritz, M.; Praus, P.; Koci, K. Unconventionally prepared TiO_2/g-C_3N_4 photocatalysts for photocatalytic decomposition of nitrous oxide. *Appl. Surf. Sci.* **2018**, *430*, 335–347. [CrossRef]
20. Sadanandam, G.; Zhang, L.; Scurrell, M.S. Enhanced photocatalytic hydrogen formation over Fe-loaded TiO_2 and g-C_3N_4 composites from mixed glycerol and water by solar irradiation. *J. Renew. Sustain. Energy* **2018**, *10*, 034703. [CrossRef]

21. Hafeez, H.Y.; Lakhara, S.K.; Bellamkonda, S.; Rao, G.R.; Shankar, M.V.; Bahnemann, D.W.; Nappolian, B. Construction of ternary hybrid layered reduced graphene oxide supported g-C_3N_4-TiO_2 nanocomposite and its photocatalytic hydrogen production activity. *Int. J. Hydrog. Energy* **2018**, *43*, 3892–3904. [CrossRef]
22. Han, C.; Wang, Y.; Lei, Y.; Wang, B.; Wu, N.; Shi, Q.; Li, Q. In situ synthesis of graphitic-C_3N_4 nanosheet hybridized N-doped TiO_2 nanofibers for efficient photocatalytic H_2 production and degradation. *Nano Res.* **2015**, *8*, 1199–1209. [CrossRef]
23. Huang, Z.; Sun, Q.; Lv, K.; Zhang, Z.; Li, M.; Li, B. Effect of contact interface between TiO_2 and g-C_3N_4 on the photoreactivity of g-C_3N_4/TiO_2 photocatalyst: (0 0 1) vs (1 0 1) facets of TiO_2. *Appl. Catal. B Environ.* **2015**, *164*, 420–427. [CrossRef]
24. Ma, J.; Tan, X.; Yu, T.; Li, X. Fabrication of g-C_3N_4/TiO_2 hierarchical spheres with reactive {001} TiO_2 crystal facets and its visible-light photocatalytic activity. *Int. J. Hydrog. Energy* **2016**, *41*, 3877–3887. [CrossRef]
25. Pan, J.; You, M.; Chi, C.; Dong, Z.; Wang, B.; Zhu, M.; Zhao, W.; Song, C.; Zhang, Y.; Li, C. The two dimension carbon quantum dots modified porous g-C_3N_4/TiO_2 nano-heterojunctions for visible light hydrogen production enhancement. *Int. J. Hydrog. Energy* **2018**, *43*, 6586–6593. [CrossRef]
26. Hao, R.; Wang, G.; Tang, H.; Sun, L.; Xu, C.; Han, D. Template-free preparation of macro/mesoporous g-C_3N_4/TiO_2 heterojunction photocatalysts with enhanced visible light photocatalytic activity. *Appl. Catal. B Environ.* **2016**, *187*, 47–58. [CrossRef]
27. Giannakopoulo, T.; Papoilias, I.; Todorova, N.; Boukos, N.; Liu, Y.; Yu, J.; Trapalis, C. Tailoring the energy band gap and edges' potentials of g-C_3N_4/TiO_2 composite photocatalysts for NOx removal. *Chem. Eng. J.* **2017**, *310*, 571–580. [CrossRef]
28. Li, J.; Zhang, M.; Li, X.; Li, Q.; Yang, J. Effect of the calcination temperature on the visible light photocatalytic activity of direct contact Z-scheme g-C_3N_4-TiO_2 heterojunction. *Appl. Catal. B Environ.* **2017**, *212*, 106–114. [CrossRef]
29. Liu, C.; Wang, F.; Zhang, J.; Wang, K.; Qiu, Y.; Liang, Q.; Chen, Z. Efficient Photoelectrochemical Water Splitting by g-C_3N_4/TiO_2 Nanotube Array Heterostructures. *Nano Micro Lett.* **2018**, *10*, 37. [CrossRef]
30. Wang, Y.; Yang, W.; Chen, X.; Wang, J.; Zhu, Y. Photocatalytic activity enhancement of core-shell structure g-C_3N_4@TiO_2 via controlled ultrathin g-C_3N_4 layer. *Appl. Catal. B Environ.* **2018**, *220*, 337–347. [CrossRef]
31. Sheng, Y.; Wai, Z.; Miao, H.; Yao, W.; Li, H.; Zhu, Y. Enhanced organic pollutant photodegradation via adsorption/photocatalysis synergy using a 3D g-C_3N_4/TiO_2 free-separation photocatalyst. *Chem. Eng. J.* **2019**, *370*, 287–294. [CrossRef]
32. Li, C.; Lou, Z.; Yang, Y.; Wang, Y.; Lu, Y.; Ye, Z.; Zhu, L. Hollow sphere Nanoheterojunction of g-C_3N_4@TiO_2 with High Visible Light Photocatalytic Property. *Langmuir* **2019**, *35*, 779–786. [CrossRef]
33. Tan, Y.; Shu, Z.; Zhou, J.; Li, T.; Wang, W.; Zhao, Z. One-step synthesis of nanostructured g-C_3N_4/TiO_2 composite for highly enhanced visible-light photocatalytic H_2 evolution. *Appl. Catal. B Environ.* **2018**, *230*, 260–268. [CrossRef]
34. Yu, S.; Wang, Y.; Sun, F.; Wang, R.; Zhou, Y. Novel mpg-C_3N_4/TiO_2 nanocomposite photocatalytic membrane reactor for sulfamethoxazole photodegradation. *Chem. Eng. J.* **2018**, *33*, 183–192. [CrossRef]
35. Zhan, W.; Sun, L.; Han, X. Recent progress on engineering highly efficient porous semiconductor photocatalysts derived from Metal–organic frameworks. *Nano-Micro Lett.* **2019**, *11*, 1. [CrossRef] [PubMed]
36. Ma, B.; Guan, P.-Y.; Li, Q.-Y.; Zhang, M.; Zang, S.-Q. MOF-derived flower-like MoS_2@TiO_2 nanohybrids with enhanced activity for hydrogen evolution. *ACS Appl. Mater. Interfaces* **2016**, *8*, 26794–26800. [CrossRef]
37. Gu, Y.; Cheng, K.; Wu, Y.-N.; Wang, Y.; Morlay, C.; Li, F. Metal–organic framework-templated synthesis of bifunctional N-doped TiO_2–carbon nanotablets via solid-state thermolysis. *ACS Sustain. Chem. Eng.* **2016**, *4*, 6744–6753. [CrossRef]
38. Yan, B.; Zhang, L.; Tang, Z.; Al-Mamun, M.; Zhao, H.; Su, X. Palladium-decorated hierarchical titania constructed from the metal-organic frameworks NH_2-MIL-125(Ti) as a robust photocatalyst for hydrogen evolution. *Appl. Catal. B Environ.* **2017**, *218*, 743–750. [CrossRef]
39. Dan-Hardi, M.; Serre, C.; Frot, T.; Rozes, L.; Maurin, G.; Sanchez, C.; Férey, G. A New Photoactive Crystalline Highly Porous Titanium(IV) Dicarboxylate. *J. Am. Chem. Soc.* **2009**, *131*, 10857–10859. [CrossRef]
40. Dou, J.; Li, Y.; Xie, F.; Ding, X.; Wei, M. Metal–Organic Framework Derived Hierarchical Porous Anatase TiO_2 as a Photoanode for Dye-Sensitized Solar Cell. *Cryst. Growth Des.* **2016**, *16*, 121–125. [CrossRef]

41. Xiu, Z.; Alfaruqi, M.H.; Gim, J.; Song, J.; Kim, S.; Thi, T.V.; Duong, P.T.; Baboo, J.P.; Mathew, V.; Kim, J. Hierarchical porous anatase TiO_2 derived from a titanium metal–organic framework as a superior anode material for lithium ion batteries. *Chem. Commun.* **2015**, *51*, 12274–12277. [CrossRef] [PubMed]
42. Guo, Z.; Cheng, J.K.; Hu, Z.; Zhang, M.; Xu, Q.; Kang, Z.; Zhao, D. Metal-organic frameworks (MOFs) as precursors towards TiOx/C composites for photodegradation of organic dye. *RSC Adv.* **2014**, *4*, 34221–34225. [CrossRef]
43. Khaletskaya, K.; Pougin, A.; Medishetty, R.; Rösler, C.; Wiktor, C.; Strunk, J.; Fischer, R.A. Fabrication of Gold/Titania Photocatalyst for CO_2 Reduction Based on Pyrolytic Conversion of the Metal–Organic Framework NH2-MIL-125(Ti) Loaded with Gold Nanoparticles. *Chem. Mater.* **2015**, *27*, 7248–7257. [CrossRef]
44. Ye, F.; Li, H.; Yu, H.; Chen, S.; Quan, X. Hydrothermal fabrication of few-layer MoS_2 nanosheets within nanopores on TiO_2 derived from MIL-125(Ti) for efficient photocatalytic H_2 evolution. *Appl. Surf. Sci.* **2017**, *426*, 177–184. [CrossRef]
45. Liu, Z.; Wu, Y.; Chen, J.; Li, Y.; Zhao, J.; Gao, K.; Na, P. Effective elimination of As(iii) via simultaneous photocatalytic oxidation and adsorption by a bifunctional cake-like TiO_2 derived from MIL-125(Ti). *Catal. Sci. Technol.* **2018**, *8*, 1936–1944. [CrossRef]
46. Yuan, S.; Gao, Y.; Bao, J.; Zhang, Y.; Chen, W.; Fang, J.; Zhou, Y.; Wang, Y.; Zhu, W. Preparation of disk-like Pt/CeO_2-p-TiO_2 catalyst derived from MIL-125(Ti) for excellent catalytic performance. *Appl. Organomet. Chem.* **2018**, *32*, e4395. [CrossRef]
47. Gao, K.; Chen, J.; Liu, Z.; Li, Y.; Wu, Y.; Zhao, J.; Na, P. Intensified redox co-conversion of As(III) and Cr(VI) with MIL-125(Ti)-derived COOH functionalized TiO_2: Performance and mechanism. *Chem. Eng. J.* **2019**, *360*, 1223–1232. [CrossRef]
48. Valero-Romero, M.J.; Santaclara, J.G.; Oar-Arteta, L.; van Koppen, L.; Osadchii, D.Y.; Gascon, J.; Kapteijn, F. Photocatalytic properties of TiO_2 and Fe-doped TiO_2 prepared by metal organic framework-mediated synthesis. *Chem. Eng. J.* **2019**, *360*, 75–88. [CrossRef]
49. Hu, S.; Liu, M.; Li, K.; Zuo, Y.; Zhang, A.; Song, C.; Zhang, G.; Guo, X. Solvothermal synthesis of NH_2-MIL-125(Ti) from circular plate to octahedron. *CrystEngComm* **2014**, *16*, 9645–9650. [CrossRef]
50. Pawar, R.C.; Kang, S.; Park, J.H.; Kim, J.-h.; Ahn, S.; Lee, C.S. Room-temperature synthesis of nanoporous 1D microrods of graphitic carbon nitride (g-C_3N_4) with highly enhanced photocatalytic activity and stability. *Sci. Rep.* **2016**, *6*, 31147. [CrossRef]
51. Music, S.; Gotic, M.; Ivanda, M.; Popovic, S.; Twkovic, A.; Trojko, R.; Sekulic, A.; Furic, K. Chemical and micro structural properties of TiO_2 synthesized by sol-gel procedure. *Mater. Sci. Eng. B* **1997**, *47*, 33–40. [CrossRef]
52. Ohsaka, T.; Izumi, F.; Fujiki, Y. Raman spectrum of anatase, TiO_2. *J. Raman Spectrosc.* **1978**, *7*, 321–324. [CrossRef]
53. Jiang, J.; Ou-yang, L.; Zhu, L.; Zheng, A.; Zou, J.; Yi, X.; Tang, H. Dependence of electronic structure of g-C_3N_4 on the layer number of its nanosheets: A study by Raman spectroscopy coupled with first-principles calculations. *Carbon* **2014**, *80*, 213–221. [CrossRef]
54. Raziq, F.; Qu, Y.; Humayun, M.; Zada, A.; Yu, H.; Jing, L. Synthesis of SnO_2/B-P codoped g-C_3N_4 nanocomposites as efficient cocatalyst-free visible-light photocatalysts for CO_2 conversion and pollutant degradation. *Appl. Catal. B Environ.* **2017**, *201*, 486–494. [CrossRef]
55. Qiu, Y.; Xin, L.; Jia, F.; Xie, J.; Li, W. Three-Dimensional Phosphorus-Doped Graphitic-C_3N_4 Self-Assembly with NH_2-Functionalized Carbon Composite Materials for Enhanced Oxygen Reduction Reaction. *Langmuir* **2016**, *32*, 12569–12578. [CrossRef]
56. Sun, P.; Xu, R.; Zhang, W.; Zada, I.; Liu, Q.; Gu, J.; Su, H.; Zhang, Z.; Zhang, J.; Zhang, D. Photocatalyst of organic pollutants decomposition: TiO_2/glass fiber cloth composites. *Catal. Today* **2016**, *274*, 2–7. [CrossRef]
57. Irie, H.; Watanabe, Y.; Hashimoto, K. Carbon-doped Anatase TiO_2 powders as a visible-light sensitive photocatalyst. *Chem. Lett.* **2003**, *32*, 772–773. [CrossRef]
58. Zhu, B.; Xia, P.; Ho, W.; Yu, J. Isoelectric point and adsorption activity of porous g-C_3N_4. *Appl. Surf. Sci.* **2015**, *344*, 188–195. [CrossRef]
59. Mandzya, N.; Grulke, E.; Druffel, T. Breakage of TiO2 agglomerates in electrostatically stabilized aqueous dispersions. *Powder Technol.* **2005**, *160*, 121–126. [CrossRef]
60. Leong, S.; Li, D.; Hapgood, K.; Zhang, X.; Wang, H. $Ni(OH)_2$ decorated rutile TiO_2 for efficient removal of tetracycline from wastewater. *Appl. Catal. B Environ.* **2016**, *198*, 224–233. [CrossRef]

61. Cetocioglu, Z.; Ince, B.; Gros, M.; Rodriguez-Mozaz, S.; Barcelo, D.; Orhon, D.; Ince, O. Chronic impact of tetracycline on the biodegradation of an organic substrate mixture under anaerobic conditions. *Water. Res.* **2013**, *47*, 2959–2969. [CrossRef] [PubMed]
62. Hsu, L.-C.; Liu, Y.-T.; Syu, C.-H.; Huang, M.-H.; Tzou, Y.-M.; Teah, H.Y. Adsorption of tetracycline on Fe (hydr)oxides: Effects pf pH and metal cation (Cu^{2+}, Zn^{2+} and Al^{3+}) addition in various molar ratios. *R. Soc. Open sci.* **2018**, *5*, 171941. [CrossRef] [PubMed]
63. Jiang, L.; Yuan, X.; Zeng, G.; Chen, X.; Wu, Z.; Liang, J.; Zhang, J.; Wang, H.; Wang, H. Phosphorus- and Sulfur-Codoped g-C_3N_4: Facile Preparation, Mechanism Insight, and Application as Efficient Photocatalyst for Tetracycline and Methyl Orange Degradation under Visible Light Irradiation. *ACS Sustain. Chem. Eng.* **2017**, *5*, 5831–5841. [CrossRef]
64. Panneri, S.; Ganguly, P.; Mohan, M.; Nair, B.N.; Peer Mohamed, A.A.; Warrier, K.G.; Hareesh, U.S. Photoregenerable, Bifunctional Granules of Carbon-Doped g-C_3N_4 as Adsorptive Photocatalyst for the Efficient Removal of Tetracycline Antibiotic. *ACS Sustain. Chem. Eng.* **2017**, *5*, 1610–1618. [CrossRef]
65. Jiang, L.; Yuan, X.; Zeng, G.; Liang, J.; Chen, X.; Yu, H.; Wang, H.; Wu, Z.; Zhang, J.; Xiong, T. In-situ synthesis of direct solid-state dual Z-scheme WO_3/g-C_3N_4/Bi_2O_3 photocatalyst for the degradation of refractory pollutant. *Appl. Catal. B Environ.* **2018**, *227*, 376–385. [CrossRef]
66. Xu, Y.; Schoonen, M.A.A. The absolute energy positions of conduction and valence bands of selected semiconducting minerals. *Am. Miner.* **2000**, *85*, 543–556. [CrossRef]
67. Xu, F.; Zhang, L.; Cheng, B.; Yu, J. Direct Z-scheme TiO_2/NiS Core-Shell Hybrid Nanofibers with Enhanced Photocatalytic H_2-Production Activity. *ACS Sustain. Chem. Eng.* **2018**, *6*, 12291–12298. [CrossRef]
68. Liu, M.; Chen, Y.; Su, J.; Shi, J.; Wang, X.; Guo, L. Photocatalytic hydrogen production using twinned nanocrystals and an unanchored NiS_x co-catalyst. *Nat. Energy* **2016**, *1*, 16151. [CrossRef]